A multiscale model predicts the sensitivity of

Chlorella vulgaris to light and nitrogen levels

in photobioreactors

Juan D. Tibocha-Bonilla[1,2], Cristal Zuniga[2], Jared T. Broddrick[3**], Karsten Zengler[2,3,4], Rubén D. Godoy-Silva[1*].

[1]Grupo de Investigación en Procesos Químicos y Bioquímicos, Departamento de Ingeniería Química y Ambiental, Universidad Nacional de Colombia, Av. Carrera 30 No. 45-03, Bogotá, D.C. Colombia.

[2]Department of Pediatrics, University of California, San Diego, 9500 Gilman Drive, La Jolla, CA 92093-0760 USA.

[3]Department of Bioengineering, University of California, San Diego, 9500 Gilman Drive, La Jolla, CA 92093-0412 USA.

[4]Center for Microbiome Innovation, University of California, San Diego, 9500 Gilman Drive, La Jolla, CA 92093-0436 USA.

*   Corresponding author

** Current affiliation: NASA Ames Research Center, Moffett Field, CA 94035 USA.

Abstract

The maximization of lipid productivity in microalgae is crucial for the biofuel industry, and it can be achieved by manipulating their metabolism. However, little efforts have been made to apply metabolic models in a dynamic framework to predict possible outcomes to scenarios observed at an industrial scale. Here, we present a dynamic framework for the simulation of large-scale photobioreactors. The framework was generated by merging the genome-scale metabolic model of *Chlorella vulgaris* (*i*CZ843) with reactor-scale parameters, thus yielding a multiscale model. This multiscale model was employed to predict the sensitivity of growth and composition variation of *C. vulgaris* on light and nitrogen levels. Simulations of lipid accumulation quantified the tradeoff between growth and lipid biosynthesis under nitrogen limitation. Moreover, our modeling approach quantitatively predicted the dependence of microalgal metabolism on light intensity and circadian oscillations. Finally, we use the model to design a reactor irradiance profile that maximized lipid accumulation, thus achieving a lipid productivity increase of 46% at a constant intensity of 966 µE m^{-2} s^{-1}. Our modeling framework elucidated how metabolism and external factors can be combined to predict optimized parameters for industrial applications.

Key words – Photobioreactor, reactor design and optimization, microalgae, *Chlorella vulgaris*, genome-scale metabolic modeling, kinetic modeling, multiscale modeling.

Background

Microalgae are unicellular photosynthetic organisms that fix carbon dioxide (CO_2) in presence of light to obtain energy and synthesize necessary metabolic precursors for growth. Carbon fixation of microalgae can be up to ten times higher than that of plants [1,2] and accounts for about 40%

37   of the Earth's CO_2 fixation [3]. Their powerful photosynthetic activity caused microalgae to be a

38   focus of research in ecology, systems biology, and bioengineering.

39   Oleaginous microalgae are able to store lipids at levels higher than 20% w/w, which is the

40   minimum threshold for profitable production of biofuels [4,5]. *Chlorella vulgaris* has drawn

41   widespread attention, as it can intracellularly concentrate up to 50% w/w of lipids in form of

42   triacylglycerols (TAGs) [6]. Since TAGs serve as main precursors for biofuel production, *C.*

43   *vulgaris* is a promising lipid producer with potential application at industrial scale. However,

44   studies about lipid accumulation have shown that stress conditions trigger lipids accumulation at

45   the expense of decreased growth rate [6,7]. At the industrial scale, reactor lipid productivities are

46   severely limited by this tradeoff, rendering the study of the interwoven connection among

47   metabolic and physical drivers of lipid biosynthesis as a field of great significance and research

48   focus. Different efforts have been made towards manipulating microalgae metabolism, mainly by

49   varying light, nitrogen, and growth conditions [8]. Nonetheless, the maximization of lipid

50   productivity in microalgae has remained a challenge for years, due to experimentation being

51   extremely time- and resource-intensive. Therefore, computational tools appear as a promising

52   alternative, since they can assess optimal growth conditions time- and cost-effectively.

53   To date, all but one study on dynamic modeling of the growth of *C. vulgaris* have been based on

54   kinetic modeling [2,9–17]. All kinetic models are based on a black-box framework. That is, their

55   primary focus is fitting experimental data regardless of the structure of underlying phenomena.

56   These models have been crucial for the development of the chemical and biochemical industry

57   [18]; however, a more robust approach is necessary to predict not only global reactor dynamics,

58   but also intracellular metabolic capabilities, namely lipid biosynthesis.

59   Microalgal metabolism has been previously studied using genome-scale metabolic (GSM) models,

60   thus elucidating organelle functionality and pathway coupling, as well as the interactions of

61   photosynthetic pathways with the rest of the network under different light wavelengths [19,20].

62   Some studies on microalgae metabolic modeling have incorporated photon uptake [21,22],

63   enabling process optimization of light intensity and culture density at the laboratory scale [21]. In

64   recent studies, experimental time-course biomass compositions were incorporated in the GSM

65   model to predict the metabolic response to nitrogen depletion [23] and to optimize nitrate supply

66   in *C. vulgaris* [24]. Notably, GSM modeling allowed to assess metabolic crosstalk in a *C.vulgaris*

67   *and Sacharomyces cerevisiae* synthetic syntrophic community [25]. Though, there exists no

68   mathematical framework that combines these metabolic models with reactor-scale dynamics for

69   the prediction of growth of microalgae, such as *C. vulgaris,* at a scale relevant to industrial

70   applications.

71   Merging mathematical representations of phenomena at the genome and reactor scale would result

72   in a multiscale model. Separately, each mathematical representation is successful in modeling the

73   phenomenon they were based upon but cannot individually account for entire reactor dynamics.

74   For example, a genome-scale metabolic (GSM) network is a powerful tool for understanding

75   species-specific metabolism. However, without experimental input, a GSM model cannot predict

76   time-course metabolic changes, as well as reactor-scale growth.

77   Here, we generated a multiscale model that simulates time-course growth and biomass composition

78   variations using an available GSM model of *C. vulgaris (i*CZ843). The model includes light

79   attenuation and uptake, photoinhibition, nitrogen and carbon uptake kinetics, and carbon allocation

80   (carbohydrate and lipid accumulation and consumption). We then employed previously reported

81   experimental growth data under different nitrogen and light conditions to validate our predictions.

82 For the former, we employed data by Adesanya et al. [13] as reference, whereas for the latter we

83 used data by Kim et al. [14]. As different strains can have different metabolic capabilities, we

84 performed data regression and validation individually for both cases. Finally, we present the

85 model's potential for its use in reactor design and optimization by determining light profiles for

86 maximizing lipid productivity in a photobioreactor.

87 Results

88 Prediction of growth trends at two different initial nitrogen concentrations

89 So far, dynamic modeling of the growth of *C. vulgaris* has been almost entirely addressed using

90 kinetic modeling (Table 1). However, this type of modeling lacks the ability to include the effect

91 of reactor-scale dynamics on microalgal metabolism. Moreover, no model has accounted for the

92 combined effect of nutrient uptake, circadian oscillations, and light attenuation on the dynamic

93 growth and biomass composition of microalgae.

94 **Table 1. Existing models for the growth of *Chlorella vulgaris*. Early models focused on dynamic**

95 **modeling through black-box methods.**

Study (Year)	Model characteristics*								
	Type	D	CU	NU	LD	LU	CO	LA	SA
Iehana (1990) [9]	K	✓							
Wijanarko et al. (2004) [10]	K	✓	✓						
Filali et al. (2011) [11]	K	✓	✓			✓			
Concas et al. (2013) [12]	K	✓	✓		✓	✓	✓		

Reference	Type	D	CU	NU	LD	LU	CO	LA	SA
Adesanya et al. (2014) [13]	K	✓	✓	✓	✓	✓		✓	
Kim et al. (2015) [14]	K	✓			✓	✓			
Sakarika et al. (2016) [15]	K	✓	✓					✓	
Adamczyk et al. (2016) [2]	K	✓	✓						
Chan et al. (2016) [16]	K	✓	✓			✓			
Zuñiga et al. (2016) [20]	GS		✓	✓		✓			
Zuñiga et al. (2017) [6]	GS	✓	✓	✓		✓			
Mansouri et al. (2017) [17]	K	✓							
Chien-Ting Li (2019)	GS	✓	✓	✓	✓			✓	
Tibocha-Bonilla et al. (2020, this study)	MS	✓	✓	✓	✓	✓	✓	✓	✓

96 Since these methods could not account for the underlying biochemistry of the cell, high complexity models

97 were not possible. With the generation of a GSM model for *C. vulgaris*, it was possible to create a multiscale

98 model that accounts for both reactor dynamics and their impact in the phenotype of the cell.

99 * Model characteristics are abbreviated as follows: dynamic (D), carbon uptake (CU), nitrogen uptake (NU),

100 light distribution (LD), light uptake (LU), circadian oscillations (CO), lipid accumulation (LA) and starch

101 accumulation (SA). Models were classified into three types: kinetic (K), genome-scale (GS) and multiscale

102 (MS).

103 We generate a multiscale model capable of predicting this interaction by merging different

104 mathematical representations (or modules, see Fig 1A) of biological and reactor dynamics at

105 different scales. Nitrogen availability has been identified as one of the most important drivers of

106 microalgal growth, as it has a profound impact on the cellular phenotype of phototrophs [6]. To

107 validate our model's sensitivity to varying nitrogen concentration, we contrasted predictions of

108   our model to experimental data reported in a kinetic study by Adesanya et al., in which *C. vulgaris*

109   was cultivated under two different initial nitrogen concentrations (first scenario: 0.021 g L^{-1},

110   second scenario: 0.124 g L^{-1}) and macromolecular cellular contents were recorded [13] (markers

111   in Fig 1B-E).

112
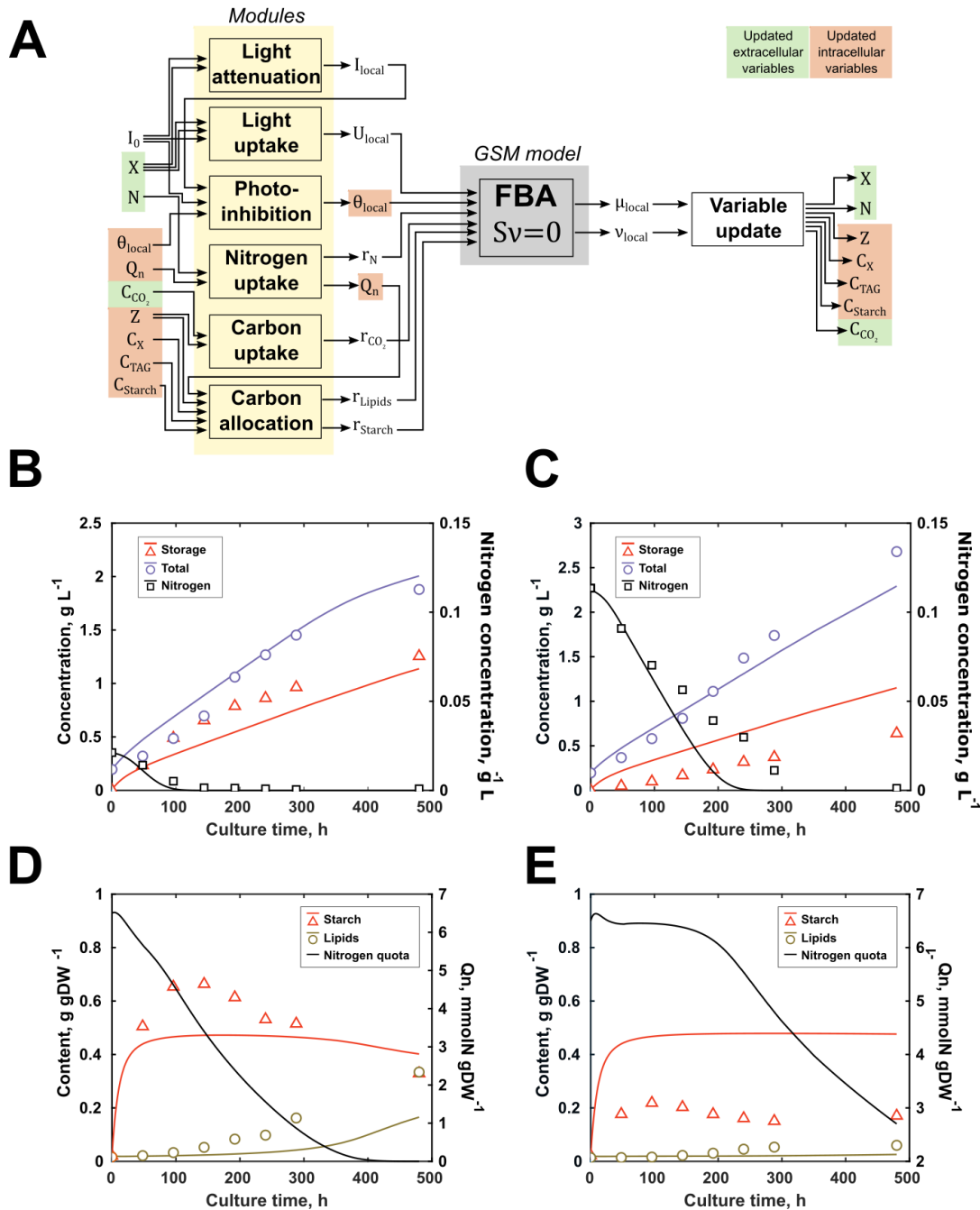
Fig 1. Simulated and reported data of *Chlorella vulgaris* at two different initial nitrogen concentrations.

(A) Schematic representation of the numerical algorithm employed in this work for a single timestep and light interval (see *Methods*). (B) and (D) correspond to the experiment with an initial nitrogen concentration of 0.021 g L^{-1}, while (C) and (E) were recorded under one of 0.124 g L^{-1}. All experiments were reported and simulated under a continuous irradiance of 80 µE m^{-2} s^{-1}. Continuous lines and markers represent predicted data by our model and reported data by Adesanya et al. [13], respectively.

We used the first scenario, with an initial nitrogen concentration of 0.021 g L^{-1} (Fig 1B & D) for the calculation of strain-specific parameters (shown in Table S1) and simulated a second scenario (Fig 1C & E) to test for predictive capability. In this scenario, a relatively low initial nitrogen concentration in the media (half that of standard BBM medium [26]) caused the size of the internal nitrogen pool to decrease steadily throughout the culture duration (Fig 1D). Since the microalga was not able to replenish its nitrogen reserves, lipid accumulation was triggered 100 h after nitrogen was depleted from the medium.

As shown in Fig 1C, under the growth conditions of the second scenario, nitrogen availability was increased six-fold. Though there were some quantitative differences regarding the starch content of *C. vulgaris*, our model was able to capture the overall trends. Our simulations show that a significant increase in the nitrogen availability allowed the microalga to replenish its nitrogen reserves for the first 200 h and caused it to deplete nitrogen from the medium 130 h later than the first scenario (Fig 1E).

The model was able to capture the almost complete inactivation of the lipid metabolism due to this nitrogen availability. However, despite there being almost no lipid accumulation and high nitrogen levels, the predicted growth rate was only amplified from an average of 0.0032 to 0.0038 h^{-1} (19% increase), similar to an experimentally determined increase of 15%.

Simulation at different light intensities

137

138 We accounted for spatial light distributions, as energy metabolism is sharply hindered for cells

139 further away from the light source, especially in larger-scale vessels. In addition, we included the

140 modeling of photoinhibition, since it restricts the maximum amount of light a culture can be

141 subjected to and the duration of exposure. Although several species have been shown to adapt to

142 high light conditions in the long term [27,28], photoinhibition still significantly diminishes the

143 growth capability of phototrophs [29–31], and specifically of *C. vulgaris* above 2400 μE m^{-2} s^{-1}

144 [32]. According to previous reports, electron transfer through the photosystems is controlled by

145 the fraction of active protein D1 of the photosystem II (PSII). Therefore, we used the model

146 proposed by Baroli et al. [30] to determine the fraction of active D1 protein as a means to penalize

147 the effective photon input to the metabolic network.

148 We employed previously reported data to validate the model's sensitivity to change in light

149 intensities. Kim et al. [14] cultured *C. vulgaris* at six different irradiances and monitored biomass

150 concentration throughout the timespan of the culture. We used data recorded at 848 μE m^{-2} s^{-1}

151 for the regression of parameters (Fig 2), while data at 30, 55, 80, 197, and 476 μE m^{-2} s^{-1} were

152 employed for model validation.

153 Experimental total biomass concentrations were recapitulated by our model. Even though

154 intracellular concentrations were not measured by Kim et al. [14], the model could be used to

155 hypothesize microscopic and macroscopic phenomena that lay underneath, e.g. circadian clock

156 oscillations, carbon allocation and responses to nitrogen depletion. As opposed to the case of

157 Adesanya et al. [13], our simulations showed that an elevated irradiance of 848 $\frac{\mu E}{m^2 s}$ made

158 impossible for the microalga to maintain the intracellular nitrogen levels after the nitrogen was

159   depleted from the medium at 100 h. This caused the lipid production to be triggered around the

160   same time point, as intracellular nitrogen levels were already decreasing sharply (Fig 2B).

161
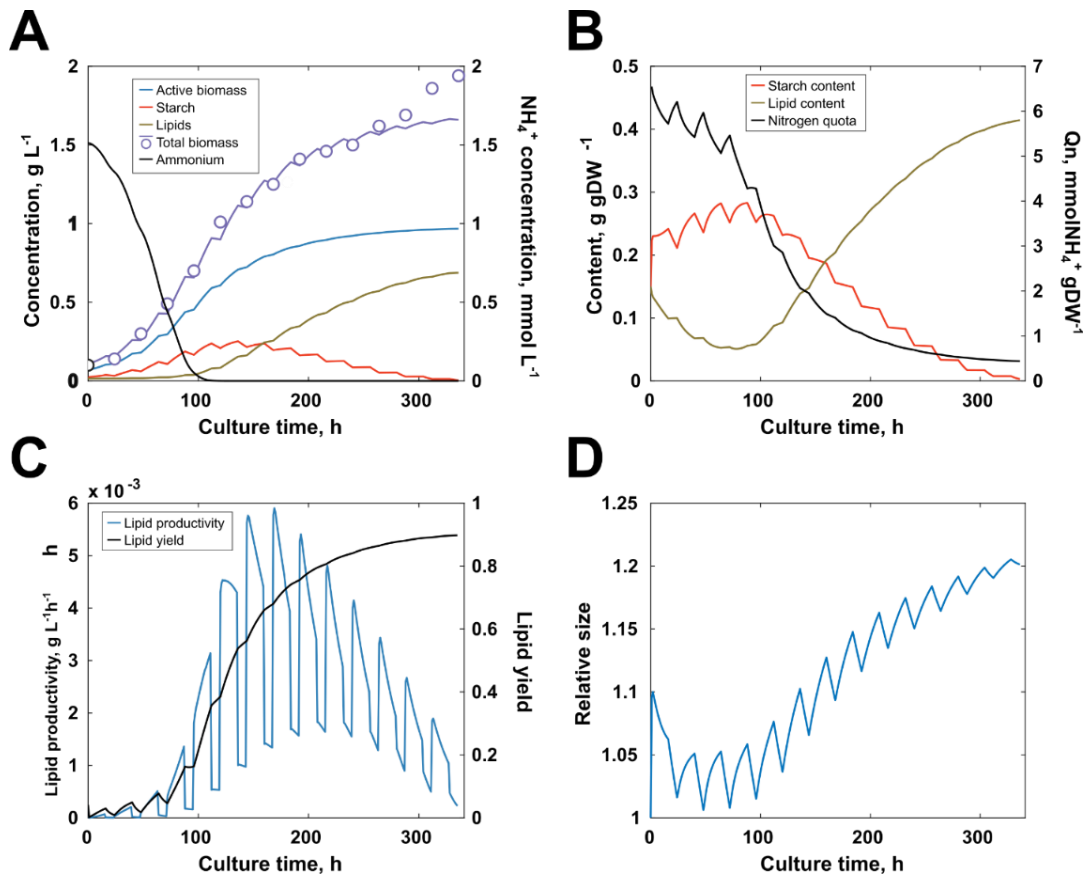
Fig 2. Contrast of calculations and reported data at 848 $\mu E\ m^{-2}\ s^{-1}$ by Kim et al [14].

163   (A) Global reactor concentrations of active (non-storage) biomass, starch, lipids, total biomass and nitrate

164   contrasted with reported data of total biomass. (B) Intracellular content of starch, lipids and nitrogen. (C)

165   Contrast of lipid productivity with lipid yield (% of carbon input directed to lipid production). (D) Variation

166   of cell size. Continuous lines and markers represent predicted data by our model and reported data,

167   respectively.

168   According to our simulations, the optimum lipid productivity was achieved shortly after nitrogen

169   was consumed from the medium but rapidly decreased afterward (Fig 2C). Interestingly, even

170   though nitrogen depletion from the medium was achieved at 100 h, peak global lipid productivity

171   of the photobioreactor took place at 168 h, when internal reserves were running low but were not

172   yet depleted. Overall lipid productivity decreased steadily for the following 167 h, as growth was

173   increasingly hindered by internal nitrogen depletion and the cell size was reaching its limit.

174   Our simulations predicted cell size change as a result of light/dark cycles and long-term nitrogen

175   depletion (Fig 2D). In general, during the light period, the cell focuses on the accumulation of

176   starch for later use under dark conditions, causing its size to increase. The opposite behavior occurs

177   during the dark period, in which starch is consumed for maintenance and growth. In the long term,

178   nitrogen depletion-induced lipid accumulation yielded bigger cells at the late stage.

179   Simulations successfully reproduced growth behavior in the photobioreactor at different irradiance

180   conditions (Fig 3). Even though they underestimated biomass production at low intensities, the

181   overall growth trends were predicted accurately. Since shading hampers the ability to fix inorganic

182   carbon, the slope of the growth curves decreased with lower irradiances. At higher intensities, it is

183   evident that an increase from 476 to 848 $\mu E\ m^{-2}\ s^{-1}$ did not signify an improvement in the overall

184   culture growth. Our simulations show that this was a consequence of a combined effect of shading,

185   photoinhibition and nitrogen limitation.

186
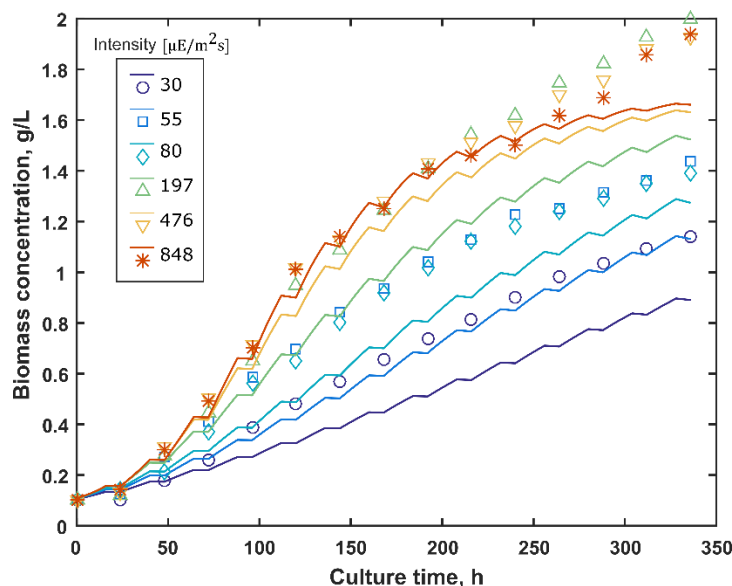
Fig 3. Growth simulation and experimental validation for different irradiance conditions reported by Kim et al. [14] at.

Lines represent model simulations while markers show reported experimental data. Even though the model underestimated growth at low intensities, growth rate response to varying light intensities was captured by the model.

Optimization of the lipid productivity in a photobioreactor

In order to illustrate the model's aptitude for process design and optimization, we predicted the optimal light strategy to maximize lipid productivity in a stirred tank photobioreactor reactor with six internal radially distributed fluorescent lamps.

In brief, five variables were manipulated to search for the optimal global lipid productivity condition: lamp irradiance at time zero I_0, lamp irradiance at the end of the culture I_f, photoperiod p, culture duration t_f, and shape of irradiance temporal profile (see *Methods*) represented by the coefficient b_I. A hypothetical base case was given to the model as the initial condition of the optimization, with an irradiance profile within the typical values previously used for experimental

201   optimization of lipid accumulation [29]. Fig S3 shows a summary of the simulation results of the

202   base case, and Table 2 summarizes the base case and optimized values of the manipulated

203   variables.

204   **Table 2. Initial and final values of the manipulated variables of the optimization.**

	I_0 $\mu E\ m^{-2}\ s^{-1}$	I_f $\mu E\ m^{-2}\ s^{-1}$	p h	t_f h	b_I
Base case	400	600	16	300	0.5
Optimized	966	966	17	374	0.0

205   Our model predicted an optimum constant irradiance of 966 $\mu E\ m^{-2}\ s^{-1}$. As shown in Fig 4, this

206   light intensity improves the final biomass concentration from 1.70 to 1.83 g/L in 374 h, which is

207   roughly a 7% increase in biomass, and 46% increase in final lipid concentration, for a 25% longer

208   culture timespan.
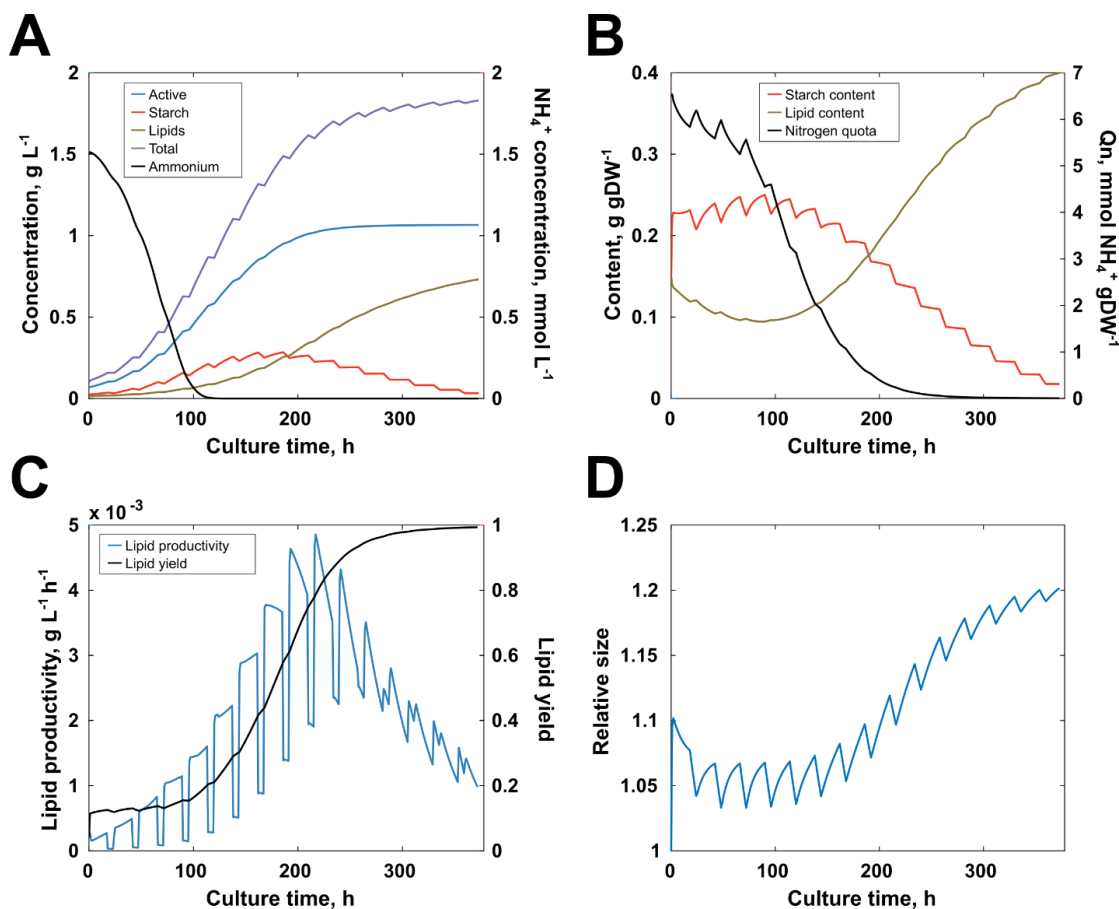
Fig 4. Simulation results of lipid productivity maximization by varying light strategy, photoperiod and culture time.

(A) Resulting optimal global reactor concentrations of active biomass, starch, lipids, total biomass and nitrate contrasted. (B) Intracellular content of starch, lipids and nitrogen. (C) Lipid productivity and lipid yield (% of carbon input directed to lipid production). (D) Variation of cell size.

Even though at the early stage of (0 – 100 h) a fraction of the culture is subjected to an irradiance of around 3,000 $\mu E\ m^{-2}\ s^{-1}$ (Fig 4), a large portion of it is under a much lower but still significant irradiance of 200 $\mu E\ m^{-2}\ s^{-1}$. This, along with high nitrogen availability, favored higher growth rates in such a way that photoinhibition was compensated. Moreover, the optimization showed that a photoperiod of 17:7 is sufficient to satisfy dark period metabolic requirements without negatively affecting growth or lipid productivity.

221   As early as 25 h into the culture, the highest irradiance inside the culture lowers to 2400

222    $\mu E\ m^{-2}\ s^{-1}$. During the medium-growth stage (100 - 200 h) shading rapidly diminished

223   photoinhibition from approximately 80% to 25%, as highest irradiances were of only 800

224    $\mu E\ m^{-2}\ s^{-1}$, and the average dropped to 200 $\mu E\ m^{-2}\ s^{-1}$.

225   At the low-growth stage (200+ h), shading is so substantial that the average irradiance drops to

226   142 $\mu E\ m^{-2}\ s^{-1}$ and stabilizes there for the rest of the culture. Moreover, as exhibited in Fig 5, at

227   this point light uptake had almost halted throughout the majority of the reactor, with an average

228   photon uptake of only 70 mmol $gDW^{-1}\ h^{-1}$, as opposed to an average of 1000 mmol $gDW^{-1}\ h^{-1}$

229   at the high-growth stage.
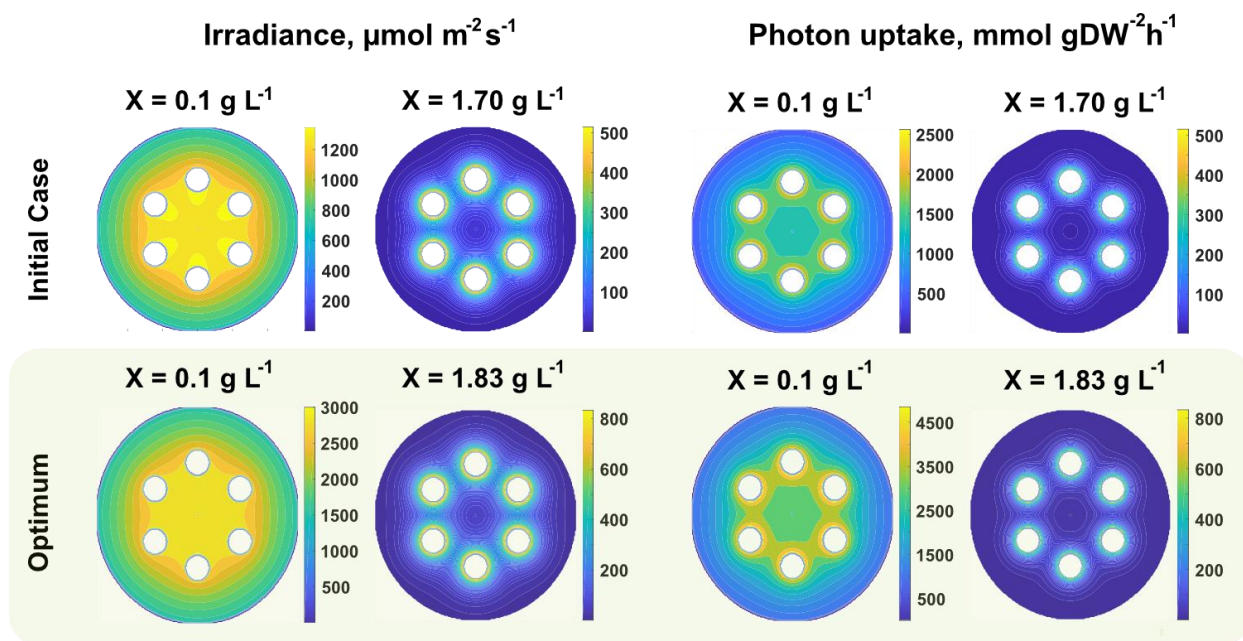
231   **Fig 5. Light and photon uptake distributions at the beginning and end of the culture.**

232   Internal cross-section distributions in the bioreactor are shown for the initial and optimum cases, at the

233   initial and final concentration. Distributions shown correspond to light intensity (irradiance) and photon

234   uptake. (Top row) Distributions for the initial case. (Bottom row) Distributions for the found optimum

235   condition.

Discussion

The multiscale model accurately predicts dynamic growth and biomass breakdown

In this work, we generated a multiscale metabolic model that predicts the growth dynamics of *Chlorella vulgaris*, by coupling mathematical representations for circadian oscillations, substrate uptake, photoinhibition and light uptake distributions. Kinetics-based dynamic metabolic modeling has already been conceived [33,34], but only Jeong et al. [35] have applied it on a complete metabolic network, and one study on a sub-network [36]. Moreover, neither study accounted for time-dependent carbon allocation or light uptake distributions.

First, we used the reported growth kinetics by Adesanya et al. [13] at two different initial nitrogen concentrations to test the model's ability to capture differential reactor behavior when nitrogen availability changed. In the first scenario, the microalga was subjected to a relatively low nitrogen availability, thus reducing its uptake rate, and preventing it from replenishing its nitrogen reserves. Consequently, lipid accumulation was triggered after nitrogen was depleted in the medium; however, its activation was not significant until days later. This implies that nitrogen depletion from the medium signifies the beginning of the end of exponential growth, rather than the end itself. A similar behavior was obtained by Mansouri et al. [17] under a comparable setup. They reported that exponential growth was maintained for the first 96 h of growth, time after which growth gradually stopped until their last recorded instance at 168 h.

A second scenario was tested in which the microalga was cultured with a six-fold increase in initial nitrogen concentration. As expected, lipid accumulation dramatically decreased in both their report and our predictions, but growth did not increase significantly (19 %). Experimental and predicted growth rates remained one order of magnitude lower than previously reported maximum growth

258 rates of 0.039 [6] and 0.033 h^{-1} [14,17]. Our simulations show that this was mainly caused by the

259 comparatively reduced irradiance as opposed to common working irradiances of 648 [6,20], 20 –

260 1400 [37], and 30 – 848 [14] $\mu E\ m^{-2}\ s^{-1}$. Low light irradiance hindered the overall growth rate

261 of the microalga, which, in addition to its higher nitrogen availability, allowed it to replenish its

262 nitrogen reserves for the most part of the culture. This relatively nitrogen-replete condition caused

263 storage molecule (lipid and starch) production to drop and rendered lipid accumulation almost

264 non-present.

265 A visible over-estimation of starch content in the second scenario was mainly caused by the

266 prioritization of starch consumption in the dark period of the topology of our carbon allocation

267 algorithm (Fig S2), which induces error when trying to predict a permanently illuminated culture,

268 as used by Adesanya et al. [13]. Further work on the generation of a multiscale model for the

269 mixotrophic growth of *C. vulgaris* will be necessary for this model to properly include starch

270 consumption in the light period, with quantitative accounting of carbon allocation and the

271 differential destination of carbon with concomitant starch breakdown and carbon dioxide

272 consumption.

273 **Light intensity drives oscillations in biomass components and cell size**

274 As a next step, we used reported data by Kim et al. [14] to show the model's capability to predict

275 the effect of varying the light intensity. Our model was able to reproduce the experimental data

276 and gave insight into the phenomena that caused the growth trends. For example, circadian clock

277 oscillations are evident in all monitored variables. Fig 2B shows the starch accumulation-

278 consumption cycles, along with a macroscopic interchange of carbon flow between starch and

279 lipids after nitrogen depletion. This behavior has previously been quantitatively determined for

280   other oleaginous microalgae, such as *Synechococcus elongatus* [38], *Chlorella sorokoniana* [39]

281   and *Dunalliela salina* [40]. In one study, *S. elongatus* exhibited a peak in ADP-glucose

282   pyrophosphorylase activity, as well as in glycerol-3-phosphate (G3P) production from ribulose

283   biphosphate (RuBP) coming from the reductive pentose-phosphate pathway (PPP) close to dawn,

284   implying high starch production in the light period [38]. The same study found the exact opposite

285   behavior in the dark, with peak activities of glycogen debranching enzyme (glgX).

286   The light-induced storage-consumption cycle is visible in the cell size variations through time,

287   where cells can be expected to increase in size in the light while storing starch and do the opposite

288   in the dark, as previously reported by Martins et al. for the cyanobacterium *Synechococcus*

289   *elongatus* [41]. Furthermore, our simulations captured the well-known tradeoff behavior between

290   specific lipid biosynthesis and growth rate, which causes the long-term cell size increase after

291   nitrogen depletion.

292   **The model can be used to design light strategies for increased lipid productivity**

293   We used the model to maximize the lipid productivity in a case of study to illustrate its potential

294   for reactor design and optimization. As opposed to previous trials on light strategies, in which

295   irradiance increases in a stair-step fashion [29], the model predicted an optimal global light

296   productivity at a constant lamp irradiance of 966 $\mu E\ m^{-2}\ s^{-1}$. At this irradiance lipid productivity

297   was predicted to increase in 46 %, despite global biomass concentration increasing by only 7%.

298   Even though the optimal irradiance is relatively high, extreme values are only reached at the early

299   stage of culture, during which high nitrogen availability favored higher growth rates in such a way

300   that photoinhibition was compensated. Moreover, during the first day of culture the highest

301   irradiance inside the culture lowered to 2400 $\mu E \, m^{-2} \, s^{-1}$, which, according to Pfendler et al. [32],

302   is the limit above which photoinhibition seriously reduces light uptake and growth in *C. vulgaris*.

303   At the late stage, shading protects most of the cells from excessive irradiances and keeps it at a

304   level that still favors metabolic activity. At this point, increasing the irradiance of the lamps would

305   hardly alter the global light availability and uptake, but would critically increase irradiance in the

306   vicinity of the lamps, where nitrogen-deplete microalgae are no longer capable of compensating

307   for photoinhibition. This means that, for this case, an individual lamp irradiance of 966 $\mu E \, m^{-2} \, s^{-1}$

308   is high enough to boost growth without excessively hindering photon uptake at all culture stages.

309   As a result, this irradiance is optimal for overall growth and lipid production in the photobioreactor.

310   In addition, it is worth noting that our model does not yet include neither the modeling of heat

311   transfer mechanisms between the lamps, medium and surroundings, nor mixing phenomena which

312   causes it to assume every cell is subjected to the same temperature. With this, the suggested

313   optimum is only attainable under a cooling system that is efficient enough to maintain overall

314   temperature between 22 – 26 °C [42].

Conclusions

316   Modeling of microalgal growth is key for the industrial production of biofuels, as it allows for the

317   design and optimization at a reactor- and whole plant-level. For this purpose, it is necessary to

318   generate a framework including accurate accounting of phenomena at every relevant scale, namely

319   at the genome scale and reactor scale. In this work, combined a GSM network with mathematical

320   representations of circadian oscillations, nutrient uptake and light distributions, which yielded a

321   comprehensive multiscale model of the growth dynamics of *Chlorella vulgaris*. We included a

322   detailed framework for the calculation of photon uptake at different irradiances, by considering

323 light attenuation and photoinhibition. The model was tested both at different nitrogen levels and

324 light irradiances, rendering it capable of being used for the prediction of specific conditions that

325 maximize lipid productivity.

Methods

327 All simulations were carried out within the MATLAB 2016b (MathWorks Inc.) environment and

328 using the COBRA Toolbox v3.0 [43]. Dynamic Flux Balance Analysis (dFBA) was used for time-

329 course flux distribution calculations and concentration updates, and GUROBI 7.5.2 was employed

330 as the solver for the linear optimization problems. A more detailed explanation of the model's

331 algorithms is shown in this section.

The multiscale metabolic model

333 At the core of our calculations lies the genome-scale metabolic model of the oleaginous microalga

334 *Chlorella vulgaris*: *iCZ843* [20], with previously proposed modifications for both heterotrophic

335 and autotrophic growth [6,20]. Overall, the GSM was solved using COBRA Toolbox (dFBA) for

336 metabolic flux distributions. In addition, a set of additional models were included to account for

337 secondary phenomena which constrained the solution space of the Linear Programming (LP)

338 system (GSM in Fig 1A). Phenomena were included according to previous reports of specific

339 physical and physiological mechanisms significantly affecting growth. Included mechanisms were

340 light attenuation, light uptake, photoinhibition, nitrogen and carbon uptake kinetics, and carbon

341 allocation (carbohydrate and lipid accumulation and consumption). Mixing, heat and mass transfer

342 phenomena were not included in the present model. A simplified representation of the general

343 numerical algorithm is presented in Fig 1A.

Light attenuation

344

345 Several studies have focused on light attenuation of microalgae [44–49], with a few solely on

346 *Chlorella vulgaris* [44,45]. In this work, we decided to use the model for light absorption and

347 scattering proposed by Naderi et al. [45], which enabled accurate predictions of light distribution

348 at low and high cell densities. The intensity profile function is shown in Eq. (1).

$$I(r, X) = I_0 \exp\left(-r \cdot K_a \cdot X \frac{r^w}{p_k + r^w}\right) \tag{1}$$

349 For internally illuminated reactors, the distance *r* was computed as the distance between the edge

350 of the light source and any given point inside the culture. Several internal sources were accounted

351 for by taking the sum of the calculated individual light distributions. For externally illuminated

352 (jacketed) reactors *r* was calculated as the distance between the illuminated edge of the reactor and

353 any given point inside the culture. K_a represents the absorption coefficient and is a function of the

354 biomass concentration X and the maximum absorption coefficient $K_{a,max}$, as shown in Eq. (2). In

355 addition, p_k, b and w are model parameters.

$$K_a(X) = \frac{K_{a,max}}{b + X} \tag{2}$$

356 The initial intensity I_0 corresponds to either the nominal or measured intensity of the light source,

357 whichever was reported in the studies. Absorption and scattering coefficients were left unchanged

358 throughout the culture time, although further studies can compute time-specific coefficients from

359 absorption spectrum data [21].

360 For increased computation speed, we divided the photobioreactor in a finite number of zones with

361 the same light intensity and calculated the overall reaction rates as a volume-weighted average of

362 the individual intervals. The number of light intervals (N_I) were determined in a logarithmic

363   fashion, as shown in Eq. (3). Mesh dependence analyses showed that 10 active (with non-zero

364   irradiance) intervals were enough for the simulations to be independent of the number of intervals.

$$I_i = 10^{\left(I_{min} + \frac{(I_{max} - I_{min})}{N_I} * i\right)} \qquad \forall i \ni \{1, \dots, N_I\} \tag{3}$$

Light uptake

366   We defined a photon conservation balance over a differential element (Fig S1) to account for

367   spatial light uptake distribution, as shown in Eq. (4).

$$(I\,A)_r - (I\,A)_{r+\Delta r} = U\,X\,\Delta V \tag{4}$$

368   The conservation balance is readily converted to the differential equation shown in Eq. (5), and a

369   cellular uptake profile (U) is obtained in Eq. (6). The magnitude U is at this point a unit-consistent

370   input to the GSM model of the microalga, which represents the upper bound of specific photon

371   uptake rate.

$$\frac{\partial I}{\partial r} + \frac{1}{r} I + U\,X = 0 \tag{5}$$

$$U(r, X) = -\frac{1}{X} \cdot \left[\frac{\partial I}{\partial r} + \frac{1}{r} I\right] \tag{6}$$

372   A similar procedure for a planar reactor yields the homologous expression shown in Eq. (7) .

$$U(r, X) = -\frac{1}{X}\frac{\partial I}{\partial r} \tag{7}$$

Photoinhibition

374   Photoinhibition is the reduction of photosynthetic capacity in photoautotrophic organisms [50],

375   and has been proven to be controlled by the photodamage – repair dynamics of the protein D1 of

376   the photosystem II (PSII) [31,50]. Consequently, an accurate account of the fraction of available

377   photons that reach the metabolic network can be performed by determining the fraction of active

378   protein D1. Therefore, the effect of photoinhibition in the model was represented by the fraction

379   of active D1, employing the model by Han [50], with the coefficients reported by Baroli et al. [30]

380   (see Eqs. (8) and (9)). The magnitude θ represented the fraction of photons that were used by the

381   metabolic network, and is a function of time t, the first-order D1 photorepair and photodamage

382   coefficients, k_r and k_d, and light intensity I. Moreover, k_r is a function of light intensity, which

383   follows a linear behavior described by the slope m_k and intersect b_k.

$$\frac{d\theta}{dt} = k_r(1 - \theta) - k_d \, I \, \theta \tag{8}$$

$$k_d = m_k \, I + b_k \tag{9}$$

384   At every timestep and light interval, metabolic flux distributions are first calculated assuming $\theta =$

385   0. The ideal photon uptake rate is then multiplied by θ and set as the new upper boundary for

386   further calculation steps.

Nitrogen and carbon uptake kinetics

388   The uptake rate of nitrogen r_N is a function of nitrogen quota (Q_n), growth rate μ, and extracellular

389   nitrogen concentration (N), as proposed by Adesanya et al. [13] and shown in Eqs. (10) and (11).

390   Other parameters include: the minimum and maximum nitrogen quotas, q_n and q_{nm}, the maximum

391   nitrogen uptake rate v_{nm}, and nitrogen uptake half-saturation coefficient v_{nh}.

$$r_N = \frac{q_{nm} - Q_n}{q_{nm} - q_n}\left[\frac{v_{nm}\, N}{N + v_{nh}}\right] \tag{10}$$

392   A simple mass balance on including growth-induced depletion and replenishment yields Eq. (11).

$$\frac{dQ_n}{dt} = r_N - Q_n\mu \tag{11}$$

393   Similarly, we used the inorganic carbon uptake kinetics model proposed by Filali [11] to calculate

394   the maximum carbon uptake rate $r_{CO_2}^{max}$ at any given moment, as shown in Eq. (12). In this model,

395   carbon uptake is a function of the concentration of carbon dioxide C_{CO_2}, the maximum carbon

396   uptake rate from the GSM model $r_{CO_2}^{max,GSM}$, the minimum cell size Z_{min}, the size increase T,

397   biomass concentration X, and carbon uptake half-saturation coefficient K_C.

$$r_{CO_2}^{max} = r_{CO_2}^{max,GSM}\left(\frac{C_{CO_2}}{C_{CO_2} + K_C * \frac{X}{Z_{min}T}}\right) \tag{12}$$

Carbon allocation

399   Nutrient availability in the media directly alters the way carbon is distributed across the cell.

400   During nutrient-sufficient conditions, microalgae tend to allocate carbon on amino acid and nucleic

401   acid biosynthesis (herein *active biomass* or X); on the other hand, nutrient-depletion, and in general

402   stress conditions, causes metabolism to shift carbon flow towards lipid biosynthesis. In

403   photobioreactors, the nitrogen poses as bottleneck for overall growth, but also as trigger for lipid

404   accumulation [6,13,17,20,51].

405   We proposed a simple flow distribution algorithm, with cell size (Z) and nitrogen quota (Q_n) as

406   coefficients for the estimation of carbon allocation. Increased nitrogen quota favored biosynthesis

407   of active biomass and starch, whereas low nitrogen levels shifted carbon flow towards lipid

408   production. We defined a magnitude n, which played the role of a penalty function on active

409   biomass production and followed the Michaelis-Menten-type function shown in Eq. (13).

$$n = 1 - \frac{q}{q + q_h} \tag{13}$$

410 Relative intracellular nitrogen levels are represented by $q = Q_n/q_{nm}$, and q_h is the half-saturation

411 coefficient. In a similar fashion, decreased cell sizes favored the uptake of inorganic carbon and

412 the accumulation of storage molecules, while bigger cells were assumed to lower carbon uptake

413 levels, as previously reported by the studies of Taguchi et al. [52] and Thompson et al. [53].

414 Therefore, we defined a penalty function z on inorganic carbon uptake, presented in Eq. (14).

$$z = \frac{T - 1}{T_{max} - 1} \tag{14}$$

415 Where T is the size increase, calculated as a function of the intracellular content of starch (x_{starch})

416 and lipids (x_{lipid}), as shown in Eq. (15).

$$T = \frac{1}{1 - x_{starch} - x_{lipid}} \tag{15}$$

417 Finally, storage starch consumption is limited by a third penalty function based on the intracellular

418 starch concentration c_{starch} and K as a half-saturation coefficient.

$$s = \frac{c_{starch}}{c_{starch} + K} \tag{16}$$

419 In the end, the penalty functions were used to constrain the solution space of the GSM, as upper

420 or lower boundaries, as shown in Eq. (17) to (20). Every variable with superscript *max* is internally

421 calculated in the algorithm as the maximum possible value at any given time point and light

422 interval. During light and dark periods, the objective functions were, respectively, starch

423 accumulation and biomass production, following previous reports of peak activities of starch

424 production and consumption in light and dark periods, respectively [38–40]. An overview of the

425 carbon allocation algorithm is illustrated in Fig S2.

$$r_{TAG} = r_{TAG}^{max} \cdot n \tag{17}$$

$$r_{CO_2}^{light} = r_{CO_2}^{max} \cdot (1 - z) \tag{18}$$

$$r_{Starch}^{dark,max} = r_{Starch}^{max} \cdot (z) \cdot (s) \tag{19}$$

$$\mu_{light} = \mu^{max} \cdot (1 - n) \cdot (z) \tag{20}$$

Parameter estimation

Metabolic capabilities across species and even strains do not remain constant. This has been one of the most significant drawbacks when trying to generate a wide-spectrum biological model. However, in this work we were able to identify five strain-specific parameters which are assumed to be inherent in the microorganism: maximum size increase z_{max}, maximum oxygen evolution $r_{O_2}^{max}$ maximum carbon uptake $r_{CO_2}^{max}$, nitrogen quota half-saturation coefficient q_h, and starch accumulation half-saturation coefficient K. Parameter estimation was done with MATLAB Optimization Toolbox, using the *active-set* algorithm. As a result, this model is capable of predicting the macroscopic outcome of a photobioreactor under different conditions for a single strain if these parameters are known. For each study we used one of the available sets of kinetic data to calculate these parameters, specifically data at an initial nitrogen concentration of 0.021 g L^{-1} for Adesanya et al. [13] and data at an irradiance of 848 μmol m^{-2} s^{-1} for Kim et al. [14]. Regression parameter values are shown in Table S1, and a summary of all other parameters is shown in Table S2.

Maximization of lipid productivity

Five variables were manipulated to search for the optimal global lipid productivity (R_L in Eq. (21)) condition: initial lamp irradiance I_0, final lamp irradiance I_f, photoperiod p, culture duration t_f, and a coefficient b_I which represents the shape of the light profile, as shown in Eq. (22).

$$R_L = \frac{C_{Lipids}}{t_f} \tag{21}$$

$$I(t) = a_I * t^{b_I} + I_0 \tag{22}$$

In Eq. (22), only b_I is used as an optimization variables, as a_I is dependent on the variables I_0, I_f and b_I itself, as presented in Eq. (23).

$$a_I = \frac{I_f - I_0}{\left(t_f\right)^{b_I}} \tag{23}$$

Declarations

Authors' contributions

JT and RG conceived the study. JT analyzed the data; JT, CZ, JB, RG and KZ discussed the data; JT wrote the manuscript with input of all co-authors.

Acknowledgements

453   **Competing interests**

454   The authors declare that they have no competing interests.

455

456   **Availability of data and materials**

457   The datasets analyzed are included in this article. The code used for simulations is fully available

458   in the *pbr* repository at https://github.com/jdtibochab/pbr.

459   **Consent for publication**

460   Not applicable.

461   **Ethics approval and consent to participate**

462   Not applicable.

References

470   1. Chisti Y. Biodiesel from microalgae. Trends Biotechnol. 2008;26:126–31.

471   2. Adamczyk M, Lasek J, Skawińska A. CO2 biofixation and growth kinetics of *Chlorella vulgaris*

472   and *Nannochloropsis gaditana*. Appl Biochem Biotechnol. 2016;179:1248–61.

473   3. Geider RJ, DeLucia EH, Falkowski PG, Finzi A, Grime JP, Grace J, et al. Primary productivity

474   of planet earth: biological determinants and physical constraints in terrestrial and aquatic habitats.

475   Glob Chang Biol. Wiley; 2001;7 (8):849–82.

476   4. Sandeep K. Sub- and supercritical water technology for biofuels. In: Lee JW, editor. Adv

477   Biofuels Bioprod. New York: Springer; 2013. p. 147–83.

478   5. Muylaert K, Bastiaens L, Vandamme D, Gouveia L. Harvesting of microalgae: overview of

479   process options and their strengths and drawbacks. Microalgae-based biofuels Bioprod. Lisbon:

480   Woodhead Publishing; 2017. p. 113–32.

481   6. Zuñiga C, Levering J, Antoniewicz MR, Guarnieri MT, Betenbaugh MJ, Zengler K, et al.

482   Predicting dynamic metabolic demands in the photosynthetic eukaryote *Chlorella vulgaris*. Plant

483   Physiol.   American   Society   of   Plant   Biologists;   2017;176:450–62.

484   http://www.plantphysiol.org/lookup/doi/10.1104/pp.17.00605. Accessed 2017 Sep 26.

485   7. Tibocha-Bonilla JD, Zuñiga C, Godoy-Silva RD, Zengler K. Advances in metabolic modeling

486   of   oleaginous   microalgae.   Biotechnol   Biofuels.   BioMed   Central;   2018;11:241.

487   https://biotechnologyforbiofuels.biomedcentral.com/articles/10.1186/s13068-018-1244-3.

488   Accessed 2018.

489   8. Sajjadi B, Chen WY, Raman AAA, Ibrahim S. Microalgae lipid and biomass for biofuel

490   production: A comprehensive review on lipid enhancement strategies and their effects on fatty

491   acid   composition.   Renew.   Sustain.   Energy   Rev.   Pergamon;   2018.   p.   200–32.

492   https://www.sciencedirect.com/science/article/pii/S1364032118305562. Accessed 2018 Dec 1.

493   9. Iehana M. Kinetic analysis of the growth of *Chlorella vulgaris*. Biotechnol Bioeng.

494   1990;36:198–206.

495   10. Wijanarko A, Witarto AB, Soemantojo RW. Effect of photoperiodicity on CO2 fixation by

496   *Chlorella vulgaris* Buitenzorg in bubble column photobioreactor for food supplement production.

497   Makara Teknol. 2004;8:35–43.

498   11. Filali R, Tebbani S, Dumur D, Isambert A, Pareau D, Lopes F. Growth modeling of the green

499   microalga *Chlorella vulgaris* in an air-lift photobioreactor. IFAC Proc Vol. 2011;18:10603–8.

500   12. Concas A, Pisu M, Cao G. Mathematical modelling of *Chlorella vulgaris* growth in semi-batch

501   photobioreactors fed with pure CO2. Chem Eng Trans. 2013;32:1021–6.

502   13. Adesanya VO, Davey MP, Scott SA, Smith AG. Kinetic modelling of growth and storage

503   molecule production in microalgae under mixotrophic and autotrophic conditions. Bioresour

504   Technol. 2014;157:293–304.

505   14. Kim J, Lee JY, Lu T. A model for autotrophic growth of *Chlorella vulgaris* under

506   photolimitation and photoinhibition in cylindrical photobioreactor. Biochem Eng J. Elsevier B.V.;

507   2015;99:55–60. http://dx.doi.org/10.1016/j.bej.2015.03.010. Accessed 2015.

508   15. Sakarika M. Kinetic study of biomass growth and lipid synthesis of the microalga *Chlorella*

509   *vulgaris* under heterotrophic conditions and energy valorization of the produced biomass. 2016.

510   16. Chang HX, Huang Y, Fu Q, Liao Q, Zhu X. Kinetic characteristics and modeling of microalgae

511   *Chlorella vulgaris* growth and CO2 biofixation considering the coupled effects of light intensity

512   and   dissolved   inorganic   carbon.   Bioresour.   Technol.   Elsevier   Ltd;   2016.

513   http://dx.doi.org/10.1016/j.biortech.2016.01.087. Accessed 2016.

514   17. Mansouri M. Predictive modeling of biomass production by *Chlorella vulgaris* in a draft- tube

515   airlift photobioreactor. Adv Environ Technol. 2017;3:119–26.

516   18. Lee E, Jalalizadeh M, Zhang Q. Growth kinetic models for microalgae cultivation: A review.

517   Algal Res. 2015. p. 497–512.

518   19. Chang RL, Ghamsari L, Manichaikul A, Hom EFY, Balaji S, Fu W, et al. Metabolic network

519   reconstruction of *Chlamydomonas* offers insight into light-driven algal metabolism. Mol Syst Biol.

520   2011;7. http://msb.embopress.org/cgi/doi/10.1038/msb.2011.52. Accessed 2011.

521   20. Zuñiga C, Li C-T, Huelsman T, Levering J, Zielinski DC, McConnell BO, et al. Genome-scale

522   metabolic model for the green alga *Chlorella vulgaris* UTEX 395 accurately predicts phenotypes

523   under autotrophic, heterotrophic, and mixotrophic growth conditions. Plant Physiol. American

524   Society   of   Plant   Biologists;   2016;172:589–602.

525   http://www.plantphysiol.org/lookup/doi/10.1104/pp.16.00593. Accessed 2016 Sep 1.

526   21. Broddrick JT, Welkie DG, Jallet D, Golden SS, Peers G, Palsson BO. Predicting the metabolic

527   capabilities of *Synechococcus elongatus* PCC 7942 adapted to different light regimes. Metab Eng.

528   Academic   Press;   2019;52:42–56.

529   https://www.sciencedirect.com/science/article/pii/S1096717618303288?via%3Dihub.   Accessed

530   2019 Mar 1.

531   22. Broddrick JT, Rubin BE, Welkie DG, Du N, Mih N, Diamond S, et al. Unique attributes of

532   cyanobacterial metabolism revealed by improved genome-scale metabolic modeling and essential

533   gene analysis. Proc Natl Acad Sci. National Academy of Sciences; 2016;113:E8344–53.

534   http://www.pnas.org/lookup/doi/10.1073/pnas.1613446113. Accessed 2016 Dec 20.

535   23. Tibocha-bonilla JD, Kumar M, Richelle A, Godoy-silva RD, Zengler K, Zuñiga C. Dynamic

536   resource allocation drives growth under nitrogen starvation in eukaryotes. npj Syst Biol Appl.

537   Springer US; 2020;1–9. http://dx.doi.org/10.1038/s41540-020-0135-y. Accessed 2020.

538   24. Li CT, Yelsky J, Chen Y, Zuñiga C, Eng R, Jiang L, et al. Utilizing genome-scale models to

539   optimize nutrient supply for sustained algal growth and lipid productivity. npj Syst Biol Appl.

540   Nature Publishing Group; 2019;5:1–11. https://www.nature.com/articles/s41540-019-0110-7.

541   Accessed 2019 Dec 1.

542   25. Zuñiga C, Li CT, Yu G, Al-Bassam MM, Li TT, Jiang L, et al. Environmental stimuli drive a

543   transition from cooperation to competition in synthetic phototrophic communities. Nat Microbiol.

544   Springer US; 2019;4:2184–91. http://dx.doi.org/10.1038/s41564-019-0567-6. Accessed 2019.

545   26. Bold HC. The Morphology of *Chlamydomonas chlamydogama*, Sp. Nov. Bull Torrey Bot

546   Club.   Torrey   Botanical   Society;   1949;76:101.

547   https://www.jstor.org/stable/2482218?origin=crossref. Accessed 1949 Mar.

548   27. Masojídek J, Torzillo G, Koblížek M, Kopecký J, Bernardini P, Sacchi A, et al.

549   Photoadaptation of two members of the Chlorophyta (*Scenedesmus* and *Chlorella*) in laboratory

550   and outdoor cultures: Changes in chlorophyll fluorescence quenching and the xanthophyll cycle.

551   Planta. 1999;209:126–35.

552   28. Garmyn M, Young AR, Miller SA. Mechanisms of and variables affecting UVR

553   photoadaptation in human skin. Photochem Photobiol Sci. Royal Society of Chemistry;

554   2018;17:1932–40.

555   29. Sun Y, Liao Q, Huang Y, Xia A, Fu Q, Zhu X, et al. Application of growth-phase based light-

556   feeding strategies to simultaneously enhance *Chlorella vulgaris* growth and lipid accumulation.

557   Bioresour Technol. Elsevier; 2018;256:421–30. https://doi.org/10.1016/j.biortech.2018.02.045.

558   Accessed 2018.

559   30. Baroli I, Melis A. Photoinhibition and repair in *Dunaliella salina* acclimated to different

560   growth irradiances. Planta. 1996;198:640–6.

561   31. Han BP. A mechanistic model of algal photoinhibition induced by photodamage to

562   photosystem-II. J Theor Biol. 2002;214:519–27.

563   32. Pfendler S, Alaoui-sossé B, Alaoui-sossé L, Bousta F, Aleya L. Effects of UV-C radiation on

564   *Chlorella vulgaris*, a biofilm-forming alga. J Appl Phycol. Journal of Applied Phycology; 2018;

565   33. Henson MA. Genome-scale modeling of microbial metabolism with temporal and spatial

566   resolution.   2017;43:1164–71.

567   https://www.ncbi.nlm.nih.gov/pmc/articles/PMC5587135/pdf/nihms901755.pdf. Accessed 2017.

568   34. Westermark S, Steuer R. Toward Multiscale Models of Cyanobacterial Growth: A Modular

569   Approach.   Front   Bioeng   Biotechnol.   2016;4:1–24.

570   http://journal.frontiersin.org/article/10.3389/fbioe.2016.00095/full. Accessed 2016.

571   35. Jeong DH, Lee JM. Integrating flux balance analysis into microalgae growth kinetics for

572   dynamic simulation. IFAC Proc. Vol. IFAC; 2013. http://dx.doi.org/10.3182/20131218-3-IN-

573   2045.00080. Accessed 2013.

574   36. Baroukh C, Muñoz-Tamayo R, Steyer JP, Bernard O. A new framework for metabolic

575   modeling under non-balanced growth. Application to carbon metabolism of unicellular

576   microalgae.   PLoS   One.   IFAC;   2013;12:107–12.

577   http://journals.plos.org/plosone/article/file?id=10.1371/journal.pone.0104499&type=printable.

578   Accessed 2013.

579   37. Bialon J, Rath T. Growth rates and photon efficiency of *Chlorella vulgaris* in relation to photon

580   absorption   rates   under   different   LED-types.   Algal   Res.   Elsevier;   2018;31:204–15.

581   https://doi.org/10.1016/j.algal.2018.02.007. Accessed 2018.

582   38. Diamond S, Jun D, Rubin BE, Golden SS. The circadian oscillator in *Synechococcus elongatus*

583   controls metabolite partitioning during diurnal growth. Proc Natl Acad Sci. 2015;112:E1916–25.

584   http://www.pnas.org/lookup/doi/10.1073/pnas.1504576112. Accessed 2015.

585   39. Bose A, Chakraborty S. Mathematical modelling of the effects of circadian rhythm on

586   microalgal growth in phototrophic and mixotrophic cultures. Chem Eng Trans. 2016;52:955–60.

587   40. Xu Y, Ibrahim IM, Harvey PJ. The influence of photoperiod and light intensity on the growth

588   and photosynthesis of *Dunaliella salina* (chlorophyta) CCAP 19/30. Plant Physiol Biochem.

589   Elsevier Masson SAS; 2016;106:305–15. http://dx.doi.org/10.1016/j.plaphy.2016.05.021.

590   Accessed 2016.

591   41. Martins BMC, Tooke AK, Thomas P, Locke JCW. Cell size control driven by the circadian

592   clock and environment in cyanobacteria. PNAS. 2018;

593   42. Serra-Maia R, Bernard O, Gonçalves A, Bensalem S, Lopes F. Influence of temperature on

594   *Chlorella vulgaris* growth and mortality rates in a photobioreactor. Algal Res. Elsevier B.V.;

595   2016;18:352–9. http://dx.doi.org/10.1016/j.algal.2016.06.016. Accessed 2016.

596   43. Ng CY, Preciat G, Žagare A, Chan SHJ, Aurich MK, Assal DC El, et al. Creation and analysis

597   of biochemical constraint-based models: the COBRA Toolbox v3.0. 2018;

598   44. Yun YS, Park JM. Attenuation of monochromatic and polychromatic lights in *Chlorella*

599   *vulgaris* suspensions. Appl Microbiol Biotechnol. 2001;55:765–70.

600   45. Naderi G, Znad H, Tade MO. Investigating and modelling of light intensity distribution inside

601   algal photobioreactor. Chem Eng Process Process Intensif. Elsevier; 2017;122:530–7.

602   https://doi.org/10.1016/j.cep.2017.04.014. Accessed 2017.

603   46. Salleh SF, Kamaruddin A, Uzir MH, Mohamed AR, Shamsuddin AH. Modeling the light

604   attenuation phenomenon during photoautotrophic growth of A. variabilis ATCC 29413 in a batch

605   photobioreactor. J Chem Technol Biotechnol. 2017;92:358–66.

606   47. Suh IS, Lee SB. A light distribution model for an internally radiating photobioreactor.

607   Biotechnol Bioeng. 2003;82:180–9.

608   48. Csögör Z, Herrenbauer M, Schmidt K, Posten C. Light distribution in a novel photobioreactor

609   - Modelling for optimization. J Appl Phycol. 2001;13:325–33.

610   49. Csögör Z, Herrenbauer M, Perner I, Schmidt K, Posten C. Design of a photo-bioreactor for

611   modelling purposes. Chem Eng Process Process Intensif. 1999;38:517–23.

612   50. Han BP, Virtanen M, Koponen J, Straskraba M. Effect of photoinhibition on algal

613   photosynthesis: a   dynamic   model.   J   Plankton   Res.   2000;22:865–85.

614   https://academic.oup.com/plankt/article-lookup/doi/10.1093/plankt/22.5.865. Accessed 2000.

615   51. Lv JM, Cheng LH, Xu XH, Zhang L, Chen HL. Enhanced lipid production of *Chlorella*

616   *vulgaris* by adjustment of cultivation conditions. Bioresour Technol. Elsevier Ltd;

617   2010;101:6797–804. http://dx.doi.org/10.1016/j.biortech.2010.03.120. Accessed 2010.

618   52. Taguchi S. Relationship Between Photosynthesis and Cell Size of Marine Diatoms. J. Phycol.

619   1976. p. 185–9.

620   53. Thompson PA, Harrison PJ, Parslow JS. Influence of irradiance on cell volume and carbon

621   quota for ten species of marine phytoplankton. J. Phycol. 1991. p. 351–60.

622